JOURNAL OF SPACECRAFT AND ROCKETS
Vol. 41, No. 5, September–October 2004

Unstructured Multigrid Simulations of Turbulent Launch Vehicle Flows Including a Propulsive Jet

Daniel Strauss*
Instituto Tecnológico de Aeronáutica, 12228-900 São José dos Campos, Brazil
and
João Luiz F. Azevedo†
Instituto de Aeronáutica e Espaço, 12228-904 São José dos Campos, Brazil

A study of the flowfield around axisymmetric launch vehicles in different flight conditions is performed. In particular, the first Brazilian Satellite Launcher second-stage configuration is analyzed considering the case with and without a propulsive jet in the vehicle base. The study is performed using a cell-centered finite volume formulation on unstructured grids. Different spatial discretization schemes are compared, including a centered and an upwind scheme. The upwind scheme is a second-order version of the Liou flux vector-splitting scheme. Turbulence effects are accounted for using two one-equation turbulence closure models, namely, the Baldwin and Barth and the Spalart and Allmaras models. An agglomeration multigrid algorithm is used to accelerate the converge to steady state of the numerical solutions. The numerical results obtained are compared with experimental data, as well as with previous structured grid simulations.

Nomenclature

A_i^+	=	turbulence model constants
$\boldsymbol{C}(\boldsymbol{Q}_i)$	=	convective operator
c_i	=	turbulence model constants
$\boldsymbol{D}(\boldsymbol{Q}_i)$	=	dissipation operator
d	=	distance to wall
$\boldsymbol{E}^{(i)}, \boldsymbol{F}^{(i)}$	=	inviscid flux vectors
$\boldsymbol{E}^{(v)}, \boldsymbol{F}^{(v)}$	=	viscous flux vectors
e	=	total energy
f_i	=	turbulence model damping functions
$\boldsymbol{H}$	=	axisymmetric source term
M_∞	=	freestream Mach number
P	=	production term
p	=	static pressure
$\boldsymbol{Q}$	=	vector of conserved variables
q_r, q_z	=	heat flux vector components
Re	=	Reynolds number
$\tilde{R}_T$	=	turbulent Reynolds number
r	=	radial coordinate
S	=	surface
t	=	time
u_r	=	Cartesian component of the velocity vector in the r direction
u_z	=	Cartesian component of the velocity vector in the z direction
V	=	volume
$\boldsymbol{V}$	=	velocity vector
$\boldsymbol{V}(\boldsymbol{Q}_i)$	=	viscous operator
z	=	axial coordinate
η^+	=	nondimensional wall coordinate
κ	=	von Kármán constant
μ	=	laminar dynamic viscosity coefficient
μ_t	=	turbulent dynamic viscosity coefficient
ν	=	laminar kinematic viscosity coefficient
ν_t	=	turbulent kinematic viscosity coefficient
ρ	=	density
ρ_w	=	wall density
σ_i	=	turbulence model constants
$\tau_{rr}, \tau_{rz}, \tau_{zz}$	=	components of the viscous stress tensor
τ_w	=	wall viscous stress
$\lvert\omega\rvert$	=	magnitude of the vorticity vector

Subscripts

i	=	ith volume
ik	=	edge between volumes i and k
∞	=	freestream conditions

Received 19 November 2002; revision received 25 July 2003; accepted for publication 1 August 2003.

*Graduate Student, Department of Aeronautical Engineering; currently Project Engineer, TECSIS Tecnologia e Sistemas Avançados, Ltda., 18086-390 Sorocaba, Brazil; daniel@tecsis.com.br. Member AIAA.

†Head, Aeroelasticity and Computational Fluid Dynamics Branch, Space Systems Division, Centro Técníco Aeroespacial; azevedo@iae.cta.br. Senior Member AIAA.

Introduction

IN the context of the development of computational tools for the simulation of launch vehicle flows, previous work[1–5] has treated the flowfield around the first Brazilian Satellite Launcher (VLS). Viscous turbulent flows in the forebody region,[1,2] as well as in the afterbody region[3,4] of the vehicle, were considered using a structured grid approach with centered implicit schemes and an axisymmetric formulation. Moreover, an unstructured grid approach was used to simulate inviscid flows over the VLS forebody in Ref. 5. This unstructured grid capability[5] consisted of an axisymmetric, finite volume, cell-centered solver, in which a centered and an upwind scheme were implemented and convergence acceleration was obtained by an agglomeration multigrid procedure. The present work is, then, an extension of the existing capability toward the treatment of viscous turbulent flows over the VLS, including the forebody region and the afterbody region with and without a propulsive jet. Hence, some of the cases studied in Refs. 3–5 are analyzed again with this new implementation.

Unstructured grids allow for a much greater flexibility in terms of control of computational mesh refinement than a structured grid approach. They can provide better resolution of flow features with lower computational cost through the use of adaptive meshes. Moreover, the use of an axisymmetric formulation is indicated due to the axial symmetry of the VLS second stage and to the fact that the vehicle is designed to fly at low angles of attack. In addition, the axisymmetric formulation represents a three-dimensional flow, but it has a computational cost equivalent to a two-dimensional simulation. Because high-speed flows including shock waves are among

the flows of interest, an upwind spatial discretization scheme is employed to increase the solution accuracy. The upwind spatial discretization scheme implemented is a second-order accurate version of Liou's AUSM$^+$ scheme.[6,7] Moreover, the use of one-equation instead of algebraic turbulence closure models is necessary for the adequate solution of the flows of interest, as observed in previous work.[3,4] The two turbulence closure models used are the Baldwin and Barth[8] and the Spalart and Allmaras[9] models.

The time-stepping method used to advance the solution of the governing equations in time in the present work is a fully explicit, second-order accurate, five-stage Runge–Kutta scheme (see Ref. 10). As the problems of interest are steady-state problems, a variable time stepping option with constant Courant–Friedrichs–Lewy number has been implemented to accelerate convergence. Experimental data and results from a structured mesh solver[3,4] are used for comparisons with the present numerical simulations. Comparisons between the results obtained with the centered and the upwind spatial discretization schemes and between the results with the two turbulence closure models implemented are also presented. Solutions over the forebody and over the afterbody regions were obtained. Furthermore, the afterbody region was treated considering cases with and without a propulsive jet.

Governing Equations

The governing equations for the aerodynamic flows of interest are the azimuthal-invariant Navier–Stokes equations in cylindrical coordinates, which can be written in integral form for the case of no body rotation as

$$\frac{\partial}{\partial t}\int_V \boldsymbol{Q}\,\mathrm{d}V + \int_S (\boldsymbol{E}r\,\mathrm{d}r - \boldsymbol{F}r\,\mathrm{d}z) + \int_V \boldsymbol{H}\,\mathrm{d}V = 0 \qquad (1)$$

In this expression, $\boldsymbol{E}=\boldsymbol{E}^{(i)}-\boldsymbol{E}^{(v)}$ and $\boldsymbol{F}=\boldsymbol{F}^{(i)}-\boldsymbol{F}^{(v)}$. The definitions of $\boldsymbol{Q}, \boldsymbol{H}, \boldsymbol{E}^{(i)}, \boldsymbol{F}^{(i)}, \boldsymbol{E}^{(v)}$, and $\boldsymbol{F}^{(v)}$ are

$$\boldsymbol{Q}=\begin{Bmatrix}\rho\\ \rho u_z\\ \rho u_r\\ e\end{Bmatrix},\qquad \boldsymbol{H}=\begin{Bmatrix}0\\ 0\\ -p/r\\ 0\end{Bmatrix},\qquad \boldsymbol{E}^{(i)}=\begin{Bmatrix}\rho u_z\\ \rho u_z^2+p\\ \rho u_z u_r\\ (e+p)\,u_z\end{Bmatrix}$$

$$\boldsymbol{F}^{(i)}=\begin{Bmatrix}\rho u_r\\ \rho u_z u_r\\ \rho u_r^2+p\\ (e+p)\,u_r\end{Bmatrix},\qquad \boldsymbol{E}^{(v)}=\frac{M_\infty}{Re}\begin{Bmatrix}0\\ \tau_{zz}\\ \tau_{zr}\\ \tau_{zz}u_z+\tau_{zr}u_r-q_z\end{Bmatrix}$$

$$\boldsymbol{F}^{(v)}=\frac{M_\infty}{Re}\begin{Bmatrix}0\\ \tau_{zr}\\ \tau_{rr}\\ \tau_{zr}u_z+\tau_{rr}u_r-q_r\end{Bmatrix} \qquad (2)$$

A suitable nondimensionalization of the governing equations is assumed to write Eq. (2). In the present case, the choice of reference state proposed in Ref. 11 is adopted. In this equation, the Reynolds number is defined in its usual form as

$$Re = l\rho_\infty q_\infty/\mu_\infty \qquad (3)$$

where l is the reference length, ρ_∞ is the freestream density, q_∞ is the magnitude of the freestream velocity vector, and μ_∞ is the molecular viscosity coefficient at the freestream temperature.

With the use of a cell-centered-based finite volume scheme, the discrete conserved variable vector is defined as an average over the cell of the continuous properties. Hence, for the ith volume, the discrete property vector is

$$\boldsymbol{Q}_i = \frac{1}{V_i}\int_{V_i}\boldsymbol{Q}\,\mathrm{d}V \qquad (4)$$

The definition of the discrete vector $\boldsymbol{Q}_i$ can be used to rewrite Eq. (1), resulting in an equation that has to be numerically implemented, that is,

$$\frac{\partial}{\partial t}(V_i\boldsymbol{Q}_i) + \int_{S_i}(\boldsymbol{E}r\,\mathrm{d}r - \boldsymbol{F}r\,\mathrm{d}z) + V_i\boldsymbol{H}_i = 0 \qquad (5)$$

where $\boldsymbol{H}_i=\boldsymbol{H}(\boldsymbol{Q}_i)$.

Turbulence Modeling

The correct account for the viscous effects in the present case involves the implementation of an appropriate turbulence closure model. The turbulence closure models implemented in this work were the Baldwin and Barth[8] and the Spalart and Allmaras[9] one-equation models. These models attempt to avoid the need to compute algebraic length scales, without having to resort to more complex two-equation, or k–ε-type, models. The models were implemented in the present code precisely as described by the Baldwin and Barth original work[8] and by the Spalart and Allmaras original work[9] for the case with no laminar regions.

The extension of both models for compressible flows was obtained simply by multiplying the kinematic turbulent viscosity coefficient by the local density, as indicated in Refs. 8 and 9. Moreover, the turbulence model equation is solved separately from the other governing equations in a loosely coupled fashion.

The Baldwin and Barth model partial differential equation, observing the nondimensionalization adopted, is

$$\frac{\mathrm{D}(\nu\tilde{R}_T)}{\mathrm{D}t} = \left(c_{\varepsilon_2}f_2 - c_{\varepsilon_1}\right)\sqrt{\nu\tilde{R}_T P} + \frac{M_\infty}{Re} \times\left[\left(\nu+\frac{\nu_t}{\sigma_\varepsilon}\right)\nabla^2(\nu\tilde{R}_T) - \frac{1}{\sigma_\varepsilon}(\nabla\nu_t)\cdot\nabla(\nu\tilde{R}_T)\right] \qquad (6)$$

In Eq. (6), $(\mathrm{D}/\mathrm{D}t)() = (\partial/\partial t)() + \boldsymbol{V}\cdot\nabla()$ is the material derivative, which contains the time derivative and convective terms; the first term on the right-hand side of the equation is the production term and the terms between the brackets are the diffusion terms. This equation is solved for the $\nu\tilde{R}_T$ variable, and the eddy viscosity is calculated as

$$\mu_t = \rho\, c_\mu D_1 D_2(\nu\tilde{R}_T) \qquad (7)$$

where the damping functions $D_1$and D_2 are designed to allow the model to be used in the near-wall region and are given by

$$D_1 = 1 - \exp\left(-\eta^+/A_1^+\right) \qquad (8)$$

$$D_2 = 1 - \exp\left(-\eta^+/A_2^+\right) \qquad (9)$$

with

$$\eta^+ = \sqrt{\frac{Re}{M_\infty}\frac{\tau_w}{\rho_w}}\frac{d}{\nu} \qquad (10)$$

$$P = \nu_t\left(\frac{\partial u_i}{\partial x_j}+\frac{\partial u_j}{\partial x_i}\right) - \frac{2}{3}\nu_t\left(\frac{\partial u_k}{\partial x_k}\right)^2 \qquad (11)$$

In Eq. (11), the usual Einstein notation and sum convention are used. The components of the velocity vector and coordinate system directions are u_i and x_i, respectively. Furthermore, $\nu_t=\mu_t/\rho$ is the equivalent of a kinematic eddy viscosity.

The Spalart and Allmaras model partial differential equation, observing the nondimensionalization adopted, is

$$\frac{\mathrm{D}\tilde{\nu}}{\mathrm{D}t} = c_{b1}\tilde{S}\tilde{\nu} + \frac{M_\infty}{Re} \times\left(\frac{1}{\sigma}\left\{\nabla\cdot[(\nu+\tilde{\nu})\nabla\tilde{\nu}] + c_{b2}(\nabla\tilde{\nu})^2\right\} - c_{w1}f_w\left[\frac{\tilde{\nu}}{d}\right]^2\right) \qquad (12)$$

Again, $\mathrm{D}/\mathrm{D}t()$ is the material derivative, and the first term on the right-hand side of Eq. (12) is the production term. Moreover, the

last term of Eq. (12) is the destruction term, and the other terms are the diffusion terms. Equation (12) is solved for the variable $\tilde{\nu}$, and the eddy viscosity is calculated as

$$\mu_t = \rho \tilde{\nu} f_{v1} \tag{13}$$

where the function f_{v1} is a damping function used to treat the buffer layer and viscous sublayer properly. This function is given by

$$f_{v1} = \chi^3 \Big/ \left(\chi^3 + c_{v1}^3\right) \tag{14}$$

where

$$\chi \equiv \tilde{\nu}/\nu \tag{15}$$

The production term is based on the vorticity, and it can be written as

$$\tilde{S} \equiv S + (M_\infty/Re)(\tilde{\nu}/\kappa^2 d^2) f_{v2} \tag{16}$$

where

$$S = |\omega| = \sqrt{\Omega_{ij}\Omega_{ij}} \tag{17}$$

and the rotation tensor Ω_{ij} is given by

$$\Omega_{ij} = \frac{\partial u_i}{\partial x_j} - \frac{\partial u_j}{\partial x_i} \tag{18}$$

Spatial Discretization Schemes

The purpose of the spatial discretization scheme is to evaluate numerically the surface integral in Eq. (5). This approximation of the integral is different for the inviscid and for the viscous flux terms. In this work, although the viscous terms are always treated using a centered scheme, the inviscid terms are treated using a centered or an upwind scheme. The approximation of the integral of the inviscid flux vectors is called convective operator, which is defined as

$$\boldsymbol{C}(\boldsymbol{Q}_i) \cong \int_{S_i} \left(\boldsymbol{E}^{(i)} r \, \mathrm{d}r - \boldsymbol{F}^{(i)} r \, \mathrm{d}z\right)$$

$$= \sum_{k=1}^{n} \left[\boldsymbol{E}_{ik}^{(i)} r_{ik} \Delta r_{ik} - \boldsymbol{F}_{ik}^{(i)} r_{ik} \Delta z_{ik}\right] \tag{19}$$

Similarly, the approximation of the integral of the viscous flux vectors is called the viscous operator, and is defined as

$$\boldsymbol{V}(\boldsymbol{Q}_i) \cong \int_{S_i} \left(\boldsymbol{E}^{(v)} r \, \mathrm{d}r - \boldsymbol{F}^{(v)} r \, \mathrm{d}z\right)$$

$$= \sum_{k=1}^{n} \left[\boldsymbol{E}_{ik}^{(v)} r_{ik} \Delta r_{ik} - F_{ik}^{(v)} r_{ik} \Delta z_{ik}\right] \tag{20}$$

For the centered scheme, the convective operator can be written as

$$\boldsymbol{C}(\boldsymbol{Q}_i) = \sum_{k=1}^{n} \left[\boldsymbol{E}^{(i)}(\boldsymbol{Q}_{ik})\, r_{ik} \Delta r_{ik} - \boldsymbol{F}^{(i)}(\boldsymbol{Q}_{ik})\, r_{ik} \Delta z_{ik}\right] \tag{21}$$

where $\boldsymbol{Q}_{ik}$ is the arithmetic average of the conserved properties in the cells that share the ik interface and n is the number of edges that form the ith control volume. The terms Δr_{ik}, Δz_{ik}, and r_{ik} are calculated as

$$\Delta r_{ik} = r_{n2} - r_{n1}, \qquad \Delta z_{ik} = z_{n2} - z_{n1}$$

$$r_{ik} = (r_{n1} + r_{n2})/2 \tag{22}$$

where (z_{n1}, r_{n1}) and (z_{n2}, r_{n2}) are the vertices that define the interface between cells i and k. A schematic representation of the node and edge nomenclature is presented in Fig. 1.

The spatial discretization procedure presented in Eq. (21) is equivalent to a central difference scheme. Therefore, artificial dissipation terms must be added to control nonlinear instabilities.[12] In the present case, the artificial dissipation operator is formed as a blend of undivided Laplacian and biharmonic operators.[10,13] Moreover, the scaling terms of the artificial dissipation model were implemented following two approaches: Jameson and Mavriplis's work[12] and Mavriplis's work.[13]

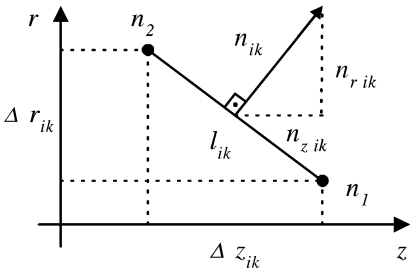

Fig. 1 Node and edge nomenclature.

The Liou[6,7] scheme implementation follows the work in Refs. 5 and 14 for both the first- and second-order version of the scheme. The second-order scheme is obtained by following exactly the same formulation of the first-order version, except that the left and right states are obtained by a MUSCL extrapolation of primitive variables.[15] In Ref. 14, a one-dimensional stencil normal to the control volume edge is constructed to obtain the extrapolated interface properties. In this work, cell-averaged property gradients are computed and used to calculate the extrapolated properties,[16] which is a different approach from that used in Ref. 14. With the property extrapolation, the state variables are represented as piecewise linear within each cell, instead of piecewise constant. Hence, to avoid oscillations in the solution due to the property extrapolation, it is necessary to use a limiter. The minmod limiter was implemented, following the work in Ref. 16. Moreover, the limiter value is frozen after a certain number of iterations to obtain a better convergence rate, as described in Ref. 17.

A centered discretization scheme was also used for the viscous operator, such that it can be written as

$$\boldsymbol{V}(\boldsymbol{Q}_i) = \sum_{k=1}^{n} \left[\boldsymbol{E}^{(v)}\left(\boldsymbol{Q}_{ik}, \left(\frac{\partial \boldsymbol{Q}}{\partial x_j}\right)_{ik}\right) r_{ik} \Delta r_{ik} - \boldsymbol{F}^{(v)}\left(\boldsymbol{Q}_{ik}, \left(\frac{\partial \boldsymbol{Q}}{\partial x_j}\right)_{ik}\right) r_{ik} \Delta z_{ik}\right] \tag{23}$$

In the preceding expression, $\boldsymbol{Q}_{ik}$ is, again, the arithmetic average of the conserved properties in the cells that share the ik interface and $(\partial \boldsymbol{Q}/\partial x_j)_{ik}$ is the arithmetic average of the conserved properties derivatives in the cells that share the ik interface. These derivatives are computed in each volume considering that the discrete derivative in a given volume is the average on the volume of the derivative and then using Green's theorem to transform the computation of the derivative into the computation of a line integral.

Multigrid Implementation

The agglomeration multigrid[18] procedure was selected among the different options for multigrid implementation on unstructured meshes.[10,13,18] This approach does not present the mesh limitations of a nested grid approach[10] nor the complexity of the calculation of the mesh intersections on a nonnested grid approach.[10,13] Moreover, it provides a fully automatic generation of the coarse meshes in such a way that only the fine mesh has to be provided as input data. Furthermore, the agglomeration multigrid approach maintains the convergence acceleration characteristics of the other multigrid procedures.

Because an agglomeration multigrid strategy was selected, the coarse meshes for the multigrid procedure are generated by agglomerating or grouping fine mesh volumes to form one coarse mesh volume. A "seed" volume is chosen in the fine mesh and, then, all of the volumes that have a node or an edge in common with this seed volume are grouped, and they form the coarse mesh volume. Another seed volume is selected, and the agglomeration procedure

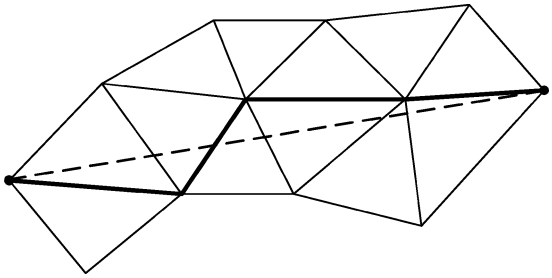

Fig. 2 Mesh simplification by the node elimination procedure.

continues grouping all of the fine mesh volumes. Note that during the agglomeration procedure only the volumes that have not been already agglomerated may be grouped to form a coarse mesh volume. This is a necessary condition to guarantee that there is no volume overlapping in the coarse mesh.

Better coarse mesh quality can be obtained if the selection of the seed volumes is not random. Therefore, a list containing all of the fine mesh volumes is generated before the agglomeration procedure. In this work, the list is formed such that the first entries are the volumes next to a boundary. This approach is very simple, easy to implement, and adds very little computational cost. Although it does not necessarily provide the best agglomeration of the interior volumes, it results in good-quality coarse mesh volumes close to the boundaries.

Because the spatial discretization scheme used in this work is linear, a simplification can be made in the coarse meshes. This simplification consists in eliminating the nodes that belong to only two volumes. The justification for this procedure comes from that the flux passing between the two volumes is the same whether the boundary separating the two volumes is discretized by one or many edges, provided that the discretization scheme is linear. Therefore, a significant amount of storage space can be saved by performing this mesh simplification. An example of such node elimination is presented in Fig. 2, where the darker lines represent the original boundary separating two coarse volumes and the dashed line represents the boundary edge after the node elimination.

Although the mesh simplification described earlier can reduce the total storage space required by the code, it brings a complication related to the connectivity of the nodes in the mesh. Because some nodes in the mesh are not used, it is necessary to ensure that the remaining nodes are properly counterclockwise oriented to have the normal vectors of each edge correctly pointing outward. This is accomplished using the node orientation in the fine mesh volumes to direct the ordering of the nodes in the coarse mesh volumes.

The agglomeration procedure can be summarized, then, in three steps. The first step consists in defining the list of volumes of the fine mesh. In the second step, the fine mesh volumes are agglomerated to form the coarse mesh volumes, following the list generated in the first step. During this step, the mesh simplification described is adopted, and only the nodes that belong to three or more coarse mesh volumes are stored. The third and final step is the verification of the node orientation in each volume of the coarse mesh and the correction of the orientation where it is needed. The actual implementation of this agglomeration procedure was designed to require the minimum amount of storage possible. Therefore, the only extra information that has to be stored in each mesh, besides the usual information associated with the solution procedure, is the number of the coarse mesh volume that contains each of the fine mesh volumes.

In the multigrid procedure, the restriction operator transfers a variable from a fine mesh to a coarse mesh. The operator used in the present work for the conserved property restriction is the volume-weighted average. Therefore, the restricted conserved properties of a coarse mesh volume are equal to the sum of the conserved properties of all of the fine mesh cells that form this coarse mesh volume, weighted by their volumes. On the other hand, the restriction of the residuals is accomplished by simple addition of the fine mesh residuals. Hence, the residual of a coarse mesh volume is equal to the sum of the residuals of all of the fine mesh volumes that are contained by this coarse mesh volume. The restriction operator for the residuals is different from the restriction operator for the conserved properties because the residuals can be interpreted as line integrals in finite volume schemes. Consequently, as the residuals of the fine mesh are summed, the interior edge contributions will cancel each other, leaving only the contribution of the edges that form the coarse mesh volume.

The prolongation operator, in opposition to the restriction operator, transfers a variable from a coarse mesh to a fine mesh. As usual with typical multigrid implementation, only the conserved property corrections have to be prolonged. Hence, only one prolongation operator has to be defined. In this work, an averaging operator was used to obtain the corrections in the fine grids. The averaging operator consists in, for each edge of the fine mesh, arithmetically averaging the corrections of the coarse mesh volumes corresponding to the two volumes that contain the edge. For each volume, then, these averaged corrections are summed, and the result is divided by the number of edges of the volume. This operator is very easy to implement, and it has the advantage of being able to transfer a linear distribution with less error than a direct injection prolongation operator.

Results and Discussion

The computational mesh used in the forebody cases is presented in Fig. 3, as well as the corresponding agglomerated meshes used for the multigrid procedure. Although this mesh is composed of quadrilateral cells and could be used in a structured mesh approach, the authors emphasize that this mesh was treated in a fully unstructured

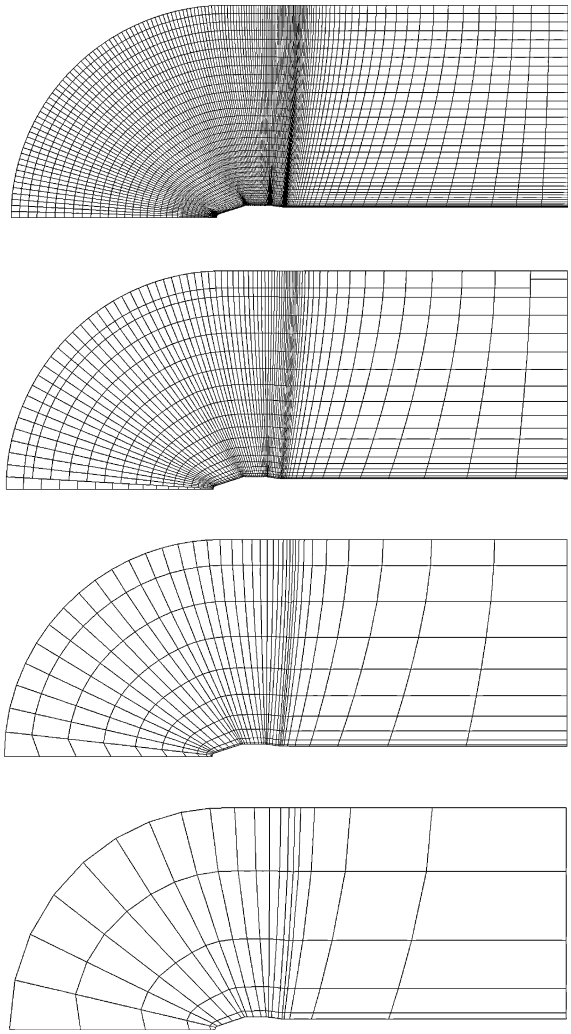

Fig. 3 Computational mesh for VLS forebody and three agglomerated meshes obtained from this mesh.

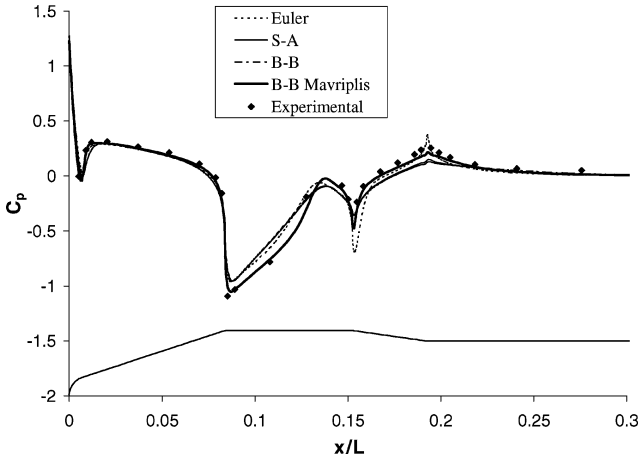

Fig. 4 Comparison of pressure coefficient distributions with the centered scheme; $M_\infty = 0.90$ and $Re = 20 \times 10^6$; Jameson and Mavriplis's artificial dissipation model used unless otherwise stated.

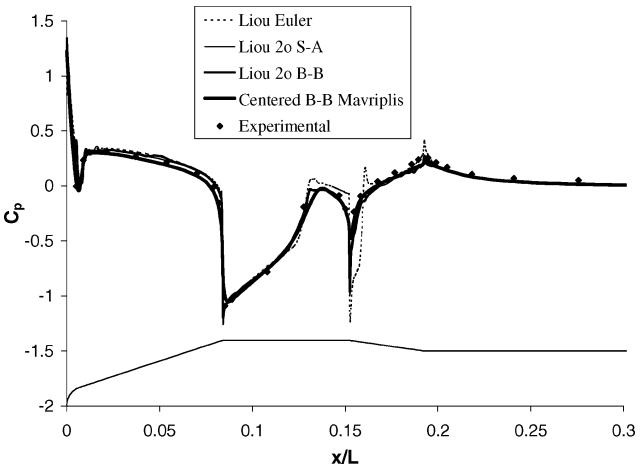

Fig. 5 Pressure coefficient distributions with Liou's second-order scheme, $M_\infty = 0.90$ and $Re = 20 \times 10^6$.

fashion. Actually, the computational grids used in the present work are the same used in Refs. 3–5 to allow a direct comparison between the present results and the results obtained in these references. Moreover, the grids used in the forebody simulations follow the guidelines of Refs. 1 and 2 in which a detailed study of the effect of various grid parameters, such as number of points, stretching, and distance of the first point off the wall, on the accuracy of the numerical solutions was performed.

A comparison of pressure coefficient distributions over the VLS for the cases using the centered scheme and both the Baldwin and Barth[8] and the Spalart and Allmaras[9] turbulence closure models is presented in Fig. 4. This case considers $M_\infty = 0.90$ and viscous turbulent flow with $Re = 20 \times 10^6$. In Fig. 4, the Baldwin and Barth model results are indicated by B-B, whereas the Spalart and Allmaras model results are indicated by S-A. Moreover, for the simulations shown in Fig. 4, the Jameson and Mavriplis artificial dissipation model[12] is used in all cases except for one, in which the Mavriplis model[13] is used. The pressure coefficient distribution for the Euler case presented in Ref. 5 is also shown in Fig. 4. The results for both the Baldwin and Barth and Spalart and Allmaras turbulence closure models are very similar, and they are also similar to the Euler results. Nevertheless, the viscous turbulent cases do not present the overexpansion and overcompression shown by the Euler results at the forebody cylinder–boattail intersection region and at the boattail–afterbody cylinder intersection region, respectively. Moreover, the results using the Mavriplis artificial dissipation model instead of the Jameson and Mavriplis model are in better agreement with the experimental results than the other results presented in Fig. 4. This behavior is to be expected because the Mavriplis artificial dissipation terms are weighted by the maximum characteristic speed in the direction normal to the control volume edge. Such construction of the artificial dissipation terms adds a more controlled amount of numerical dissipation to the scheme, and hence, it yields better results.

The results obtained with Liou's spatial discretization scheme and both the Baldwin and Barth and the Spalart and Allmaras models are presented in Fig. 5. The corresponding results for the inviscid case, presented in Ref. 5, as well as the results with the centered scheme with the Mavriplis artificial dissipation model, presented in Fig. 4, are also shown in Fig. 5. The solution with the centered scheme and the Mavriplis artificial dissipation model is very close to the solution with Liou's scheme, as one can see in Fig. 5. However, a comparison of flowfield property contours indicates that the solution with Liou's scheme provides a sharper representation of the shock waves and expansion regions, and it also showed better agreement with experimental flow visualization schlieren photographs.[5] The flow visualization figures are not included here because a similar behavior was already observed with the inviscid calculations reported in Ref. 5. Hence, despite the slight tendency of presenting spikes at compression and expansion corners, the turbulent calculations with the Liou scheme provide numerical results that seem to be in better overall agreement with the experimental data. Moreover, similarly to the behavior observed with the centered scheme, the results with the turbulence models do not present the dramatic overexpansions and overcompressions observed in the inviscid results.

Fig. 6 Turbulent viscosity contours for the case with Liou's second-order scheme and Spalart and Allmaras model, $M_\infty = 0.90$ and $Re = 20 \times 10^6$.

Another important result obtained for the viscous turbulent case is the turbulent viscosity distribution on the flowfield. Hence, the turbulent viscosity contours for the case using Liou's spatial discretization scheme and the Spalart and Allmaras turbulence closure model are presented in Fig. 6. In Fig. 6, one can observe that meaningful values of turbulent viscosity are concentrated in the boundary layer close to the body, where the shear stresses are relevant. Moreover, the boundary layer thickens from the forebody to the afterbody. This behavior is exactly the expected one for this case. A result similar to that of Fig. 6 was obtained with the Baldwin and Barth turbulence closure model, although some oscillations in the turbulent viscosity were observed at the edge of the boundary layer. The y^+ value for the first grid point off the wall in this case was of the order of 0.6 throughout the complete forebody region. For the turbulence models here contemplated, it is believed that this value of y^+ is adequate.

The mesh used to obtain the last results presented for the VLS was the mesh presented in Fig. 3. As already mentioned, this mesh was generated from a structured mesh. This structured mesh was, then, used to obtain numerical results for the same case with $M_\infty = 0.90$ and $Re = 20 \times 10^6$ but using the structured grid code developed in Refs. 3, 4, and 19. A comparison between the structured and the unstructured results is shown in Fig. 7. Both results were obtained using the centered spatial discretization scheme and the Baldwin and Barth turbulence closure model. The result corresponding to the unstructured mesh shown in Fig. 7 is the same result presented in Fig. 4 for the case using the Mavriplis artificial dissipation model. From the comparison presented in Fig. 7, one can see that the results using both mesh approaches are very similar. This was expected because, besides the mesh topology, a similar formulation was used in both cases. Moreover, the unstructured mesh results are in a slightly better agreement with the experimental data.

The afterbody of the VLS second stage is treated initially as a simple base, that is, without a propulsive jet at the vehicle base. This case considers a freestream Mach number of 0.5 and a Reynolds number of 20×10^6. Moreover, the centered scheme with the Mavriplis artificial dissipation model is used, and the turbulent effects are accounted for by the Baldwin and Barth turbulence closure model. The mesh used in this case is presented in Fig. 8, and it is an extension of the forebody mesh show in Fig. 3 that also includes the afterbody region. This mesh has a grid point concentration near the base region to capture the boundary layer close to this wall. Studies of grid refinement and grid topology were carried out in Refs. 4 and 19. In Refs. 4 and 19, the authors show that adequate refinement and grid stretching, both in the streamwise and crossflow directions, are of fundamental importance to capture correctly the flow structures that appear in the base region and in the jet. Because the present work used the same final meshes reported in Refs. 4 and 19, the authors did not repeat the complete mesh refinement study in the current case. Furthermore, one of the objectives of the present effort is to compare the unstructured grid results here reported with the previous structured calculations in Refs. 4 and 19. The pressure contours in the afterbody region for this case are presented in Fig. 9. These contours are very similar to the ones obtained in Refs. 3 and 19 with the structured grid solver for the same case and using the same turbulence model formulation.

The results shown in Fig. 9 reproduce the general trend of the expected behavior of the flow. The flow detaches from the body at the base edge and forms a recirculation bubble in the near wake. This separated region ends in a stagnation point downstream of the base. The flowfield described can be seen in Fig. 10, in which a streamline plot of the near wake with the separated region is shown. A quantitative comparison of the results with experimental data is presented in Table 1, in terms of the axial position of the rear stagnation point. The position is measured along the centerline from the vehicle base and is presented nondimensionalized by the afterbody diameter. The experimental data were obtained from Ref. 20 for cylindrical afterbodies, and the errors obtained in the numerical results are of approximately 13%. These errors are not completely unexpected because the authors of Ref. 20 indicate that the near-wake development is dependent on the flow conditions approaching the separation point. Therefore, because the forebody in the present work is different from the one used in the experiments of Ref. 20, the boundary layer in the proximity of the separation point is also different, resulting in the differences in the near wake. Moreover, the results obtained with the unstructured calculation were almost coincident with the ones obtained with the structured grid approach.

The cases that include a base with a propulsive jet considered in this work are always of underexpanded sonic or supersonic jets, and the expected jet structure is presented in Fig. 11. Expansion waves propagate downstream from the jet exit, resulting in a jet area increase. These expansion waves reflect at the centerline as compression waves and cause a jet area reduction farther downstream. The area increase is consistent with the jet acceleration because the jet is sonic or supersonic. Moreover, the area reduction causes a jet deceleration, which is achieved by a normal shock wave, also called a Mach disk. A system of oblique shock waves also forms to adjust the flow direction next to the jet boundaries. After the Mach disk,

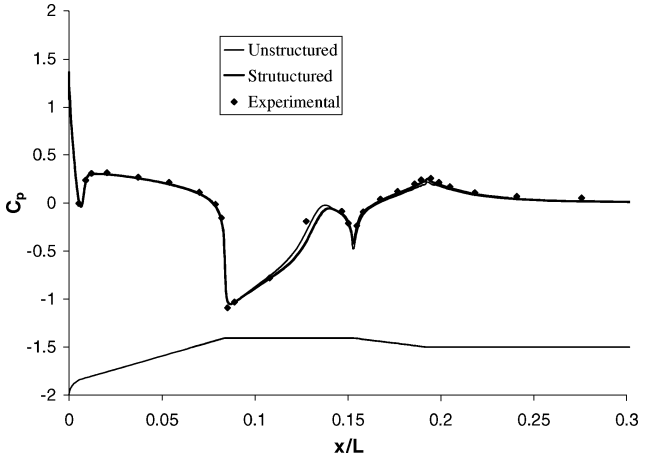

Fig. 7 Comparison of pressure coefficient distributions with previous structured results, $M_\infty = 0.90$ and $Re = 20 \times 10^6$.

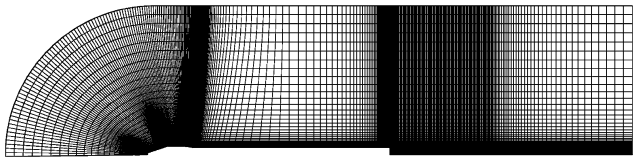

Fig. 8 Computational mesh including the VLS afterbody region.

Table 1 Position of rear stagnation point behind the body base[a]

Case description	Position, x/D[b]
Present unstructured results	1.39
Previous structured results[19]	1.37
Experimental data[20]	1.21

[a] $M_\infty = 0.5$ and $Re = 20 \times 10^6$.
[b] D is the afterbody diameter and x is measured from the body base along the downstream centerline.

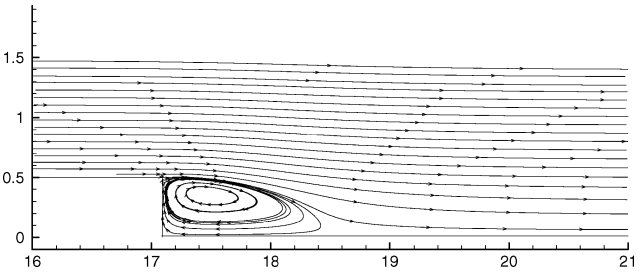

Fig. 10 Streamlines in the afterbody region for case without propulsive jet, $M_\infty = 0.50$ and $Re = 20 \times 10^6$.

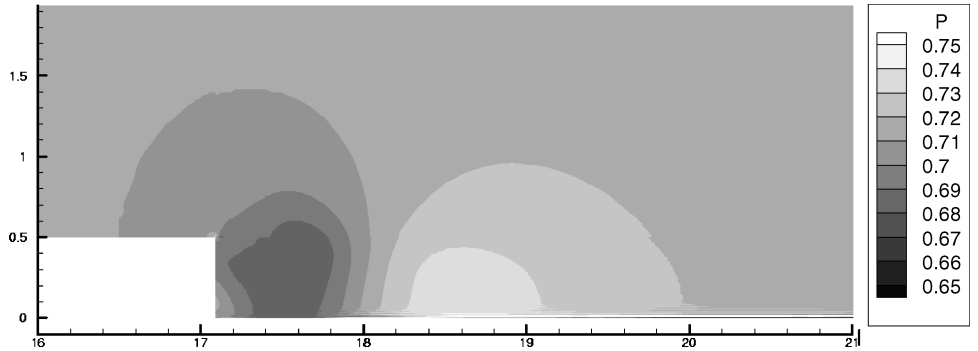

Fig. 9 Pressure contours in the VLS afterbody region without propulsive jet, $M_\infty = 0.50$ and $Re = 20 \times 10^6$.

the flow is subsonic and, therefore, accelerates as a result of the area reduction, until it becomes sonic again. After that, depending on the jet-to-freestream pressure ratio, the complete jet structure repeats itself.

The parameters indicated in Fig. 11 are used to compare the numerical and the experimental results. These parameters are diameter of the jet exit, d, initial inclination of the jet boundary δ, crossflow diameter of the normal shock wave or Mach disk, S, position of the normal shock wave, l, and length of the first periodic structure, w. However, note that this is the structure of a freejet. The presence of a high-speed freestream flow can change this structure because the freestream flow can inhibit the jet expansion. Because most of the experimental results found in the literature are for jets discharging in still air, some tests with very low freestream Mach numbers were performed for comparison. However, the real interest of this work is on supersonic freestream conditions; thus, cases with these conditions will also be shown. The computational mesh used for the jet cases is presented in Fig. 12, which shows only the afterbody region. This mesh has essentially the same number of grid points as the one shown in Fig. 8, except that it has a more uniform point distribution in the afterbody region, with less refinement in the near wake in the direction normal to the base.

To simulate freejet conditions, a freestream Mach number equal to zero should be used. However, the nondimensionalization adopted yields terms that are divided by the freestream Mach number, and therefore, M_∞ cannot be equal to zero to avoid numerical problems. Hence, $M_\infty = 0.01$ was chosen for the freejet cases. The Mach number contours for a case, with $M_\infty = 0.01$, $M_{\text{jet}} = 1.0$, $p_{\text{jet}} = 10 p_\infty$, and $T_{\text{jet}} = T_\infty$ is shown in Fig. 13. In this case, as well as in all cases considering a propulsive jet, the Liou spatial discretization scheme was used. Moreover, the Baldwin and Barth turbulence closure model was used to capture properly the turbulence effects. An excellent qualitative agreement has been obtained between the numerical solution and the expected jet structure shown in Fig. 11. A very good quantitative agreement was also obtained, as one can see in Table 2. The experimental results shown in Table 2 were obtained from Ref. 21. Discrepancies between the present computational results and the experimental data are usually less than 13% for all parameters analyzed.

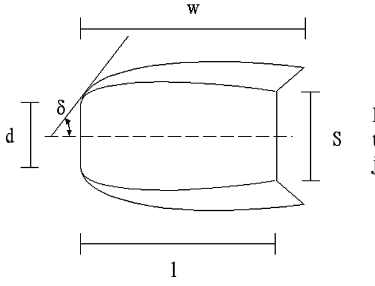

Fig. 11 Expected jet structure in immediate vicinity of jet exit.

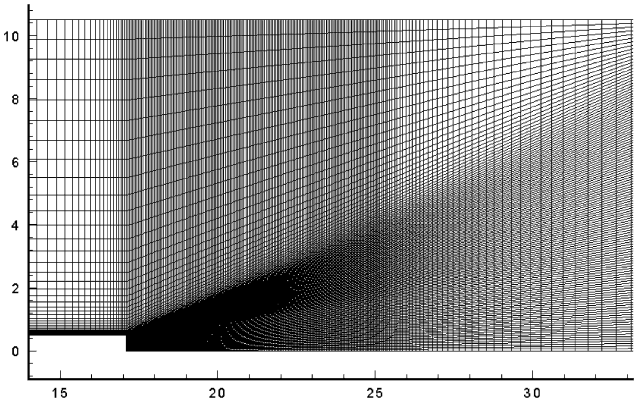

Fig. 12 Computational mesh in the afterbody region for the cases including propulsive jet on vehicle base.

The freestream conditions considered for the first case run including a propulsive jet on the vehicle base and a nonstill freestream were Mach number of 0.5 and Reynolds number of 20×10^6. The jet conditions adopted in this case were Mach number of 1.0 and static pressure and temperature three and two times, respectively, the corresponding freestream quantities. The Mach number contours in the base region for this case are presented in Fig. 14. In Fig. 14, a jet structure very similar to the expected one, presented in Fig. 11, can be observed, showing a very good qualitative comparison with experimental results. Furthermore, this case was also run in Refs. 4 and 19 using a structured grid approach, and the results obtained in the present work were very similar to the ones shown in those references.

Flow conditions, which are representative of the actual VLS flight regimes, were also simulated. In this test, the corresponding freestream and jet properties result in more complex flowfields and represent a more severe simulation case. The flow properties that are representative for the VLS second-stage flight conditions are $M_\infty = 4.9$, $M_{\text{jet}} = 4.0$, $p_{\text{jet}} = 112.0\ p_\infty$, $T_{\text{jet}} = 4.6\ T_\infty$, and $Re = 20 \times 10^6$. The Mach number contours for this case are shown in Fig. 15. Observe that the jet expansion is very large in this case, and the plume structure seems to be similar to what can be observed, for instance, in Fig. 14. However, the computational domain does not extend far enough downstream to capture the normal shock and all of the downstream portions of the plume structure. Nevertheless, from the point of view of the accuracy of the solutions here presented, this should not cause any problems because the flowfield is completely supersonic throughout the entire exit plane. Therefore, whatever flow structures are supposed to appear downstream of the computational exit plane cannot influence the present computational domain. Furthermore, as one could expect, the very high

Table 2 Comparison of the jet parameters with experimental results for a jet discharging in still air[a]

Case description	w/d	l/d	S/d	δ, deg
Present unstructured results	3.8	3.1	1.22	35.7
Previous structured results[4,19]	3.7	3.1	1.64	44.6
Experimental data[21]	3.6	2.9	1.40	40.2

[a] $M_{\text{jet}} = 1.0$, $p_{\text{jet}} = 10\ p_\infty$, and $T_{\text{jet}} = T_\infty$.

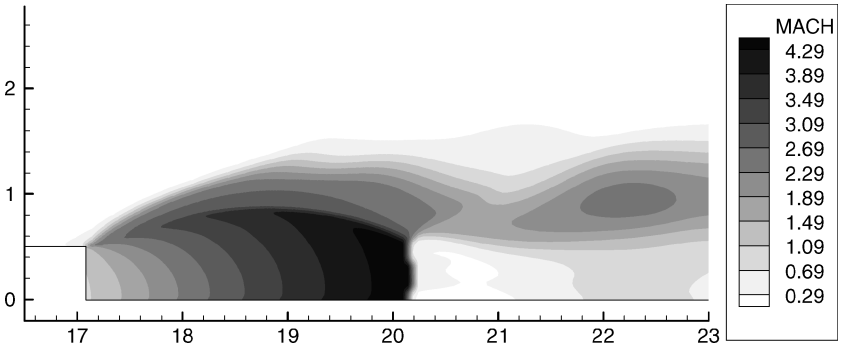

Fig. 13 Mach contours in the base region for freejet case; $M_\infty = 0.01$, $M_{\text{jet}} = 1.0$, $p_{\text{jet}} = 10\ p_\infty$, $T_{\text{jet}} = T_\infty$, and $Re = 20 \times 10^6$.

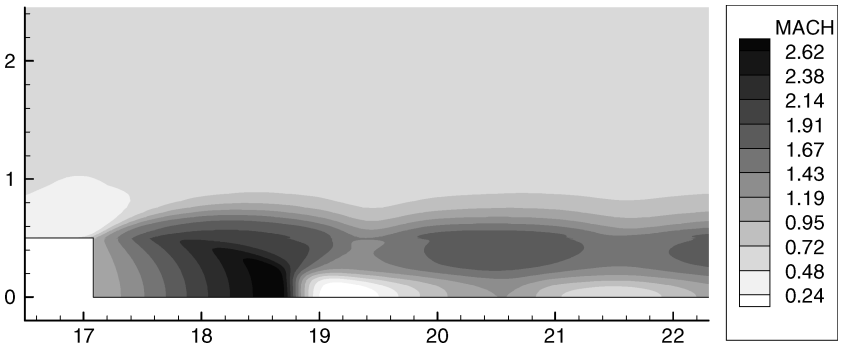

Fig. 14 Mach number contours in the base region for the case including propulsive jet; $M_\infty = 0.5, M_{jet} = 1.0, p_{jet} = 3\,p_\infty, T_{jet} = 2\,T_\infty$, and $Re = 20 \times 10^6$.

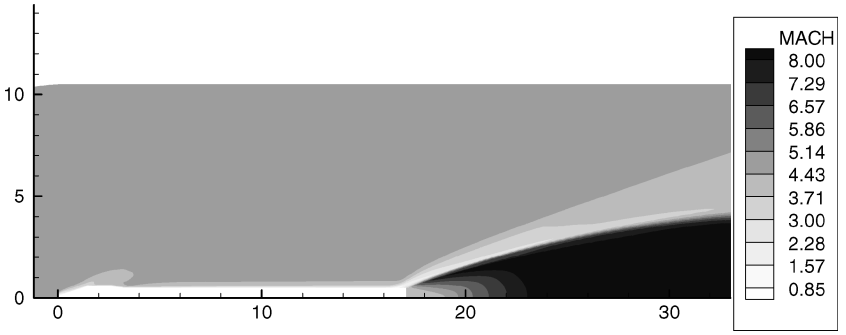

Fig. 15 Mach number contours for the VLS second-stage flight conditions; $M_\infty = 4.9, M_{jet} = 4.0, p_{jet} = 112.0\,p_\infty, T_{jet} = 4.6\,T_\infty$, and $Re = 20 \times 10^6$.

jet-to-freestream static pressure ratio results in a strong expansion downstream of the jet exit, with local Mach numbers within the jet core reaching values as high as 12. The full range of Mach numbers within the jet is not represented in the labels of Fig. 15 to allow the reader to see some other features of the flow. Moreover, the rapid jet expansion at its exit station causes the formation of an oblique shock wave in the external flow right at the afterbody edge. This feature can also be seen in Fig. 15.

Conclusions

The transonic flowfield around the VLS forebody was studied using a viscous turbulent formulation. Comparisons between the numerical results obtained and the experimental data showed very good agreement in terms of pressure coefficient distribution, as well as in terms of the flow features. The results with the turbulence models obtained in the present work do not present the overexpansion and overcompression observed in the inviscid results of previous work. Moreover, the solutions obtained with the Liou scheme were in slight better agreement with the experimental results than those obtained with the centered scheme. Furthermore, the solutions with the centered scheme and the Mavriplis artificial dissipation model were closer to the solution with the Liou scheme than the solution with the centered scheme and the Jameson and Mavriplis artificial dissipation model.

Afterbody simulations considered cases with and without a propulsive base jet. The results without a propulsive jet of the present work were compared with previous structured grid results obtained by the authors and with experimental data for general cylindrical afterbodies at zero angle of attack. The present unstructured grid results were essentially equal to the structured grid results. Moreover, the computational results reproduced the experimental data in terms of the location of the rear stagnation point. The discrepancies between computational and experimental values for this parameter were at most of 13%.

For the cases with a propulsive jet, because the majority of the data in the literature are concerned with freejets, the simulations initially performed considered jets discharging in a still atmosphere. Because of specific details of code implementation, this was simulated considering an external freestream with $M_\infty = 0.01$. An extremely good qualitative agreement was obtained with the available experimental results for freejets and the quantitative comparison of results also indicated good agreement with the available data. Discrepancies between the present computational results and the experimental data were less than 13% for all parameters analyzed. Results with a nonzero freestream Mach number also indicated a very good qualitative agreement with the type of behavior that should be expected in this case. Although there was no experimental data to compare the present results, as in the freejet cases, the solution structures were essentially the same ones observed in the freejet cases. Furthermore, the results obtained, which also included realistic VLS second-stage flight conditions, were also compared with the structured grid cases of previous work by the authors, and, again, very good agreement was obtained with these results. Therefore, the contribution of the present work rests mainly on the development of a simulation capability that allowed the treatment of realistic flowfields of interest for the aerodynamic analysis of general satellite launcher configurations. In particular, this capability has been applied to a detailed study of axisymmetric VLS flows, which has added to the understanding of the aerodynamics of this vehicle.

Acknowledgment

The authors gratefully acknowledge the partial support of Conselho Nacional de Desenvolvimento Científico e Tecnológico under Integrated Project Research Grant 522413/96-0.

References

[1]Azevedo, J. L. F., Menezes, J. C. L., and Fico, N. G. C. R., Jr., "An Assessment of Boundary Layer Properties for Transonic and Supersonic Flows Over the VLS," *Proceedings of the 13th AIAA Applied Aerodynamics Conference*, Pt. 1, AIAA, Washington, DC, 1995, pp. 41–51.

[2]Azevedo, J. L. F., Menezes, J. C. L., and Fico, N. G. C. R., Jr., "Accurate Turbulent Calculations of Transonic Launch Vehicle Flows," *Proceedings of the 14th AIAA Applied Aerodynamics Conference*, Pt. 2, AIAA, Reston, VA, 1996, pp. 841–851.

[3]Azevedo, J. L. F., Strauss, D., and Ferrari, M. A. S., "Viscous Multiblock Simulations of Axisymmetric Launch Vehicle Flows," *Journal of Spacecraft and Rockets*, Vol. 36, No. 4, 1999, pp. 489–498.

[4]Strauss, D., and Azevedo, J. L. F., "A Numerical Study of Turbulent Afterbody Flows Including a Propulsive Jet," *Proceedings of the 17th AIAA Applied Aerodynamics Conference*, AIAA, Reston, VA, 1999, pp. 654–664.

[5]Strauss, D., and Azevedo, J. L. F., "Unstructured Multigrid Simulations of Axisymmetric Inviscid Launch Vehicle Flows," AIAA Paper 2001-2476, June 2001.

[6]Liou, M.-S., "A Continuing Search for a Near-Perfect Numerical Flux Scheme. Part I: AUSM$^+$," NASA TM-106524, March 1994.

[7]Liou, M.-S., "A Sequel to AUSM: AUSM$^+$," *Journal of Computational Physics*, Vol. 129, No. 2, 1996, pp. 364–382.

[8]Baldwin, B. S., and Barth, T. J., "A One-Equation Turbulence Transport Model for High Reynolds Number Wall-Bounded Flows," NASA TM-102847, Nov. 1990.

[9]Spalart, P. R., and Allmaras, S. R., "A One-Equation Turbulence Model for Aerodynamic Flows," *La Recherche Aérospatiale*, No. 1, 1994, pp. 5–21; also AIAA Paper 92-0439, Jan. 1992.

[10]Mavriplis, D. J., "Multigrid Solution of the Two-Dimensional Euler Equations on Unstructured Triangular Meshes," *AIAA Journal*, Vol. 26, No. 7, 1988, pp. 824–831.

[11]Pulliam, T. H., and Steger, J. L., "Implicit Finite-Difference Simulations of Three-Dimensional Compressible Flow," *AIAA Journal*, Vol. 18, No. 2, 1980, pp. 159–167.

[12]Jameson, A., and Mavriplis, D. J., "Finite Volume Solution of the Two-Dimensional Euler Equations on a Regular Triangular Mesh," *AIAA Journal*, Vol. 24, No. 4, 1986, pp. 611–618.

[13]Mavriplis, D. J., "Accurate Multigrid Solution of the Euler Equations on Unstructured and Adaptive Meshes," *AIAA Journal*, Vol. 28, No. 2, 1990, pp. 213–221.

[14]Azevedo, J. L. F., and Korzenowski, H., "Comparison of Unstructured Grid Finite Volume Methods for Cold Gas Hypersonic Flow Simulations," *Proceedings of the 16th AIAA Applied Aerodynamics Conference*, AIAA, Reston, VA, 1998, pp. 447–463.

[15]van Leer, B., "Towards the Ultimate Conservative Difference Scheme. V. A Second-Order Sequel to Godunov's Method," *Journal of Computational Physics*, Vol. 32, No. 1, 1979, pp. 101–136.

[16]Barth, T. J., and Jespersen, D. C., "The Design and Application of Upwind Schemes on Unstructured Meshes," AIAA Paper 89-0366, Jan. 1989.

[17]Venkatakrishnan, V., "Convergence to Steady State Solutions of the Euler Equations on Unstructured Grids with Limiters," *Journal of Computational Physics*, Vol. 118, No. 1, 1995, pp. 120–130.

[18]Mavriplis, D. J., and Venkatakrishnan, V., "Agglomeration Multigrid for Viscous Turbulent Flows," AIAA Paper 94-2332, June 1994.

[19]Strauss, D., "Turbulent Multiblock Simulations of Axisymmetric Launch Vehicle Afterbody Flows," Graduation Project, Dept. of Aeronautical Engineering, Inst. Tecnológico de Aeronáutica, São José dos Campos, Brazil, Nov. 1999.

[20]Merz, R. A., Page, R. H., and Przirembel, C. E. G., "Subsonic Axisymmetric Near-Wake Studies," *AIAA Journal*, Vol. 16, No. 7, 1978, pp. 656–662.

[21]Love, E. S., Grigsby, C. E., Lee, L. P., and Woodling, M. J., "Experimental and Theoretical Studies of Axisymmetric Free Jets," NASA TR R-6, 1959.

R. M. Cummings
Associate Editor